International Communications in Heat and Mass Transfer 158 (2024) 107932

Contents lists available at ScienceDirect

International Communications in Heat and Mass Transfer

journal homepage: www.elsevier.com/locate/ichmt

Explicitly defined empirical constant for phase-change simulation in a two-phase closed thermosyphon

Sehyeon Cho [a], Dayoung Kong [b], Gyohoon Geum [a], Seungjae Lee [a], Junrae Park [a], Seong Hyuk Lee [a,c], Jungho Lee [d,*], Hyoungsoon Lee [a,c,**]

[a] Department of Intelligent Energy and Industry, Chung-Ang University, Seoul 06974, South Korea
[b] Department of Mechanical Engineering, Stanford University, Stanford, CA 94305, USA
[c] School of Mechanical Engineering, Chung-Ang University, Seoul 06974, South Korea
[d] Department of Mechanical Engineering, Ajou University, Suwon 16499, Republic of Korea

ARTICLE INFO

Keywords:
Two-phase closed thermosyphon
Explicitly defined
Phase-change model
OpenFOAM
Mass transfer intensity factor

ABSTRACT

Over several decades, the importance of energy recovery has grown because of the global shift from fossil fuels to renewable energy sources. Among various energy-recovery approaches, waste heat recovery has emerged as a prominent method owing to its ease of adoption in various fields such as power plants and commercial buildings and high amount of recovery by adopting in the heavy industry. A heat exchanger with a heat pipe offers superior waste heat recovery efficiency through its highly effective heat transfer in a two-phase closed thermosyphon (TPCT). Numerous investigations have explored the thermal hydraulic performance of TPCTs in various geometries and operation conditions, mostly relying on experimental methods owing to the challenges in accurately simulating phase change in TPCT systems. These challenges arise from using the mass-transfer intensity factor, r—an empirically selected constant in phase-change models—which lacks a robust basis in fundamental principles. This study introduces a novel approach to selecting the r value for simulating the phase-change process in TPCTs. By employing the volume-of-fluid model for multiphase interfaces along with the widely used Lee model for phase change, the proposed model establishes a correlation between evaporation and condensation mass fluxes to define the r value in condensation heat transfer within a TPCT. The utilisation of the proposed model in simulations yielded improved temperature predictions, deviating by 4–7 K from experimental results while offering a significant reduction in the number of r values to choose from, achieved by explicitly defining the r value for condensation heat transfer. The conventional approach was to set both empirical constants to $r_e = r_c = 0.1$ s^{-1}. However, this model, which provides a relationship between the two empirical constants based on mass balance, revealed that r_c should be 9.8 s^{-1} rather than 0.1 s^{-1} corresponding to $r_e = 0.1$ s^{-1}. Furthermore, the study examines the diverse thermal performance outcomes associated with varying r values for evaporation in a wide range of r_e (0.1–100 s^{-1}). r_c was in the range of 9.8–12.7 s^{-1}, denoting an increase of only 30% as r_e increased 1000 times from 0.1 to 100 s^{-1}. This research offers a comprehensive understanding of the computational modelling of TPCTs, providing valuable insights into their thermal characteristics based on the intricate phase-change phenomena occurring within them.

1. Introduction

Over the past 20 years, significant amounts of carbon dioxide have been emitted owing to the uncontrolled use of fossil fuels, accelerating global warming. Accordingly, there has been a growing interest in transitioning from fossil fuels to green energy. Green energy can be produced using various methods. However, methods based on waste-energy recovery (such as thermoelectric devices [1], piezoelectric devices [2], and waste heat recovery system [3]) has gained significant attention owing to its potential for improving energy efficiency. Among these methods, waste heat recovery is highly regarded because of its wide range of applications, high energy-recovery rates, and efficiency [4]. Waste heat recovery is primarily accomplished by capturing and utilising wasted heat energy using heat exchangers. Numerous studies have aimed at enhancing the thermal performance of heat exchangers by

* Corresponding author at: Department of Mechanical Engineering, Ajou University, Suwon, Gyeonggi-do 16499, South Korea.
** Corresponding author at: School of Mechanical Engineering, Chung-Ang University, Seoul 06974, South Korea.
E-mail addresses: jungholee@ajou.ac.kr (J. Lee), leeh@cau.ac.kr (H. Lee).

https://doi.org/10.1016/j.icheatmasstransfer.2024.107932

Available online 15 August 2024

Nomenclature

C_p	specific heat at constant pressure
C_v	specific heat at constant volume
d	diameter
g	acceleration due to gravity
h	enthalpy
h_{fg}	latent heat
I	current
k	thermal conductivity
k_{eff}	effective thermal conductivity
L	length
m	mass
n	normal
P	pressure
Q	heat transfer rate
q''	heat flux
R_{th}	thermal resistance
r	mass-transfer intensity factor
v	volume
S	source
T	temperature
T_{sat}	saturation temperature
$TPCT$	two-phase closed thermosyphon
t	time
u	velocity

Greek symbols

α	volume fraction
κ	curvature
μ	dynamic viscosity
ν	kinetic viscosity
ρ	density
σ	surface tension

Subscripts

c	condensation
e	evaporation
f	fluid
g	gas
in	inlet
out	outlet
w	wall

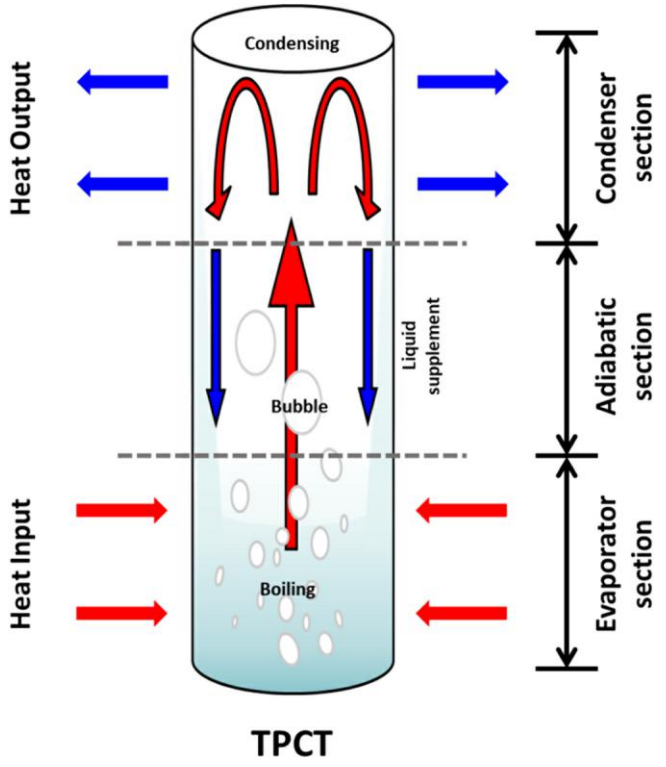

Fig. 1. Schematic diagram of the TPCT working process. The TPCT configuration includes a lower evaporator, an upper condenser, and an intervening adiabatic section. Vapour produced in the evaporator ascends to the condenser, releasing heat and condensing on the wall, and it subsequently descends under the influence of gravity.

employing diverse geometries and design types. Among these, the shell-and-tube heat exchanger stands out as being extensively applied in waste-heat-recovery systems owing to its exceptional efficiency in recovering wasted heat. Over the past few decades, various studies, including those involving finned tubes, baffles, and nanofluids [5–7], have been adopted to enhance waste-heat-recovery efficiency in shell-and-tube heat exchangers. A notable trend involves integrating a two-phase closed thermosyphon (TPCT), instead of conventional pipes, into well-engineered shell-and-tube heat exchangers, driven by the enhanced heat-transfer efficiency of the TPCT [8].

A TPCT functions as a passive device driven by gravity, eliminating the need for external driving forces. It has gained attention for its exceptional heat-transfer capabilities via phase change. Structurally, the TPCT setup comprises a lower evaporator, an upper condenser, and an adiabatic section in between. In a TPCT, which operates on the principle of heat entry through the evaporator, the working fluid undergoes vaporisation, and then the vapour, driven by density differences, rises to the condenser, where it releases heat and condenses on the condenser's wall. The resulting condensed liquid descends along the wall under gravity (Fig. 1). This process highlights the high heat-transfer efficiency of the TPCT achieved by utilising phase change. For developing the thermal performance of TPCTs, various experimental studies have been conducted on filling ratio, surface modification, and working fluid to improve the heat-transfer performance of TPCTs [9–12].

Starting from 2010, numerical approaches have been employed to investigate the thermal performance of and fluid distributions in TPCT [13–30]. The most crucial aspect in two-phase simulation is the selection of an appropriate phase-change model. This model defines the mass-transfer rate during phase change. Various phase-change models have been suggested, such as the Lee model [31], Schrage model [32], sharp-interface model [33], and energy balance model [34]. The Lee model is the simplest physical model, which summarizes various factors into a mass transfer intensity factor, r value, for evaporation and condensation. The Schrage model is a phase change model based on the Hertz–Knudsen equation allowing the temperature and pressure jump at the interface between liquid and vapour. The sharp-interface model is based on conduction heat transfer. Finally, the energy balance model is suggested for phase change considering energy balance by assuming that all the thermal energy will be used as latent heat during phase change. Most numerical investigations related to TPCT have utilised the Lee model owing to its ease of implementation in commercial computational fluid dynamics (CFD) software and its ability to achieve favourable convergence in CFD calculations. In the Lee model, the mass-transfer rate is defined using a mass-transfer intensity factor, r, which is an arbitrary or empirically chosen constant. Higher r values result in higher mass-

Table 1
Current status of computational research on TPCT.

Author(s)	Geometry (D × L) [mm^2]	Inclination [°]	Working fluid	Filling ratio	r_e [s^{-1}]	r_c [s^{-1}]	Saturation Temperature [K]	Note
Alizadehdakhel et al. (2010)	19 × 1000	90	Water	0.3–0.8	0.1	0.1	350	–
Fadhl et al. (2013)	22 × 500	90	Water	0.5	0.1	0.1	373	–
Kafeel & Khurram (2014)	39 × 980	90	Water	0.3	0.1	Eq. (c)	350	Pulsed heat flux condition
Fadhl et al. (2015)	22 × 500	90	R134a, R404a	0.5	0.1	0.1	Not specified	–
Kim et al. (2015)	22 × 500	90	Water	0.5	0.1	$r_{evap} \times (\rho_f / \rho_g)$	373	Density ratio to adopt mass transfer intensity factor
Alammar et al. (2016)	22 × 400	10–90	Water	0.25–1	0.1	0.1	373	–
Xu et al. (2016)	25.4 × 240	15–90	water	0.25	Eq. (a)	Eq. (c)	Not specified	Contact angle modelling
Jafari et al. (2017)	35 × 500	90	Water	0.16–1.35	Fine-tuned	0.16–1.35	Not specified	Unsteady thermal characteristics
Fertahi et al. (2018)	9.8 × 190	90	water	0.25	Fine-tuned	0.25	373	Externally finned geometry
Wang et al. (2018)	18 × 440	90	Water	0.75	Fine-tuned	Fine-tuned	318	Numerical modelling of geyser boiling in TPCT
Wang et al. (2019)	38 × 2000	90	Ammonia	0.2–0.3	0.02–2	$100 \times r_{evap} - 10{,}000 \times r_{evap}$	Not specified	Different heating lengths H_{evap} = 400–600 mm
Hosseinzadeh et al. (2020)	22 × 500	90	Water, 1-butanol-water	0.5	0.1	0.1	Not specified	–
Jobori and Jawad (2020)	22 × 400	15–90	Water	0.25–0.9	Eq. (b)	Eq. (d)	373	–
Yuan et al. (2020)	9.52 × 1250	90	R134a	0.8	0.1	0.1	As Experimental data	Effect of non-condensable gas
Tarokh et al. (2021)	22 × 500	90	Water	0.5	0.1	$r_e \times (\rho_f / \rho_g)$	373	Vortex generation geometry
Xiao et al. (2022)	47 × 1000	90	CuO-H_2O	0.15–0.25	Fine-tuned	0.15–0.25	Not specified	–
Present Study	20.2 × 400	90	Water	0.65	0.1–100	Eq. (e)	Function of vapour density	Different condenser lengths L_c = 50–200 mm

r_e: Eq. (a) $r_{e,old} - r_{e,old}\left\{\frac{m_e - m_c}{max(m_e, m_c)}\right\}$, Eq. (b) $\frac{6\rho_g \Delta h\sqrt{M}}{D_{sm}(\rho_f - \rho_g)\sqrt{2\pi RT_{sat}}}$, r_c: Eq. (c) $r_{c,old} - r_{c,old}\left\{\frac{m_c - m_e}{max(m_e, m_c)}\right\}$, Eq. (d) $\frac{6\rho_f \Delta h\sqrt{M}}{D_{sm}(\rho_f - \rho_g)\sqrt{2\pi RT_{sat}}}$, Eq. (e) $r_e \times \sum_1^{n.e}\left\{\frac{\alpha_l \rho_l (T - T_{sat})}{T_{sat}}\right\}_{e.cell} / \sum_1^{n.c}\left\{\frac{\alpha_v \rho_v (T_{sat} - T)}{T_{sat}}\right\}_{c.cell}$.

transfer rates, while lower values lead to decreased mass-transfer rates. For accurate TPCT simulation, precise definitions of two distinct mass-transfer intensity factors—r_e for the evaporator and r_c for the condenser—are essential, given the simultaneous involvement of both the evaporator and condenser in the TPCT.

The r values used in previous TPCT studies are summarised in Table 1. In the early 2010s, researchers utilised r values of $r_e = r_c = 0.1$ s^{-1}, as selecting a value too high caused convergence problems and opting for a value too small resulted in a considerable deviation of the local cell temperature at the interface from T_{sat} [13–18]. Alizadehdakhel et al. [13] were the first to implement the TPCT in a phase change simulation in a two-dimensional domain using the Lee model with $r_e = r_c = 0.1$ s^{-1} and studied the parameter of heat flux and filling ratio (FR), which affect the thermal performance of TPCT. Fadhl et al. [14,15] also conducted their TPCT phase change simulation using the Lee model with $r_e = r_c = 0.1$ s^{-1} to investigate the thermal performance of water, R134a, and R404a as working fluids. Yuan et al. [16] adopted their empirical constant as $r_e = r_c = 0.1$ s^{-1} to implement the Lee model and investigated the effect of a non-condensable gas on the thermal performance of TPCT. In the study of Alammar et al. [17], the conventional condition of $r_e = r_c = 0.1$ s^{-1} was employed to investigate the effect of FR by computational simulation. The r values in some studies [19–23] were fine-tuned to experimental data. Jafari et al. [19] investigated TPCT simulation with unsteady thermal characteristics and fine-tuned the empirical constants. Fertahi et al. [20] conducted phase change simulation using the Lee model to investigate the effect of externally finned geometry and selected fine-tuned empirical constants. Wang et al. [24] attempted to find the most suitable r values for the investigation of two-phase loop thermosyphon and employed the r values as $r_e = 0.1$ s^{-1} and $r_c = 10^3$ s^{-1}. Cho et al. [25] performed tests with different r values for the evaporator and condenser, exploring a wide range of values, namely, r_e = 0.025–0.075 s^{-1} and $r_c = 5 \times 10^4$–100×10^4 s^{-1}. They showed that increasing r_e values resulted in higher T_{sat}, while T_{sat} tended to decrease with increasing r_c values, Additionally, they integrated T_{sat} changes according to the mass balance into their phase-change model to improve predictive accuracy. There have been several attempts to adopt functional relations to define mass-transfer intensity factors to increase the predictive accuracy in TPCT simulations. Kim et al. [26] suggested the functional r_c based on r_e considering the density difference between liquid and gas and adopted $r_e = 0.1$ s^{-1}, $r_c = r_e \times (\rho_f / \rho_g)$ to cover the mass-transfer rate difference in terms of density difference. Tarokh et al. [27] also adopted the functional r_c based on the density difference suggested by Kim et al. [26]. Kafeel and Khurram [28] suggested the functional r_c that considers the mass-transfer rate of the previous iteration to balance the mass-transfer rate of evaporation and condensation. Xu et al. [29] employed not only the functional r_c but also the functional r_e in the equivalent method of Kafeel and Khurram [28], while Jobori and Jawad [30] selected r values considering the kinetic gas theory with

assumptions. As shown in previous relevant studies, most mass-transfer intensity factors are conventionally selected as $r_e = r_c = 0.1\ s^{-1}$ or are fine-tuned through simulations using individual experimental data. However, there remains a lack of understanding of the underlying physics when selecting r_e and r_c. This selection fails to account for density differences in the evaporator and condenser regions, often leading to a lack of mass conservation during phase change simulations or increased computational costs. Consequently, this becomes a bottleneck in improving the predictive accuracy of TPCT simulations.

In this study, a novel approach is introduced to define the mass-transfer intensity factor of the Lee model. The proposed model establishes correlations between r_e and r_c according to the mass balance. This reduces the number of empirical constants from two to one and leads to reasonable results in phase change simulations using the exact value of r_c. The study also analysed the trend of explicitly defined r_c and the corresponding wall temperature distribution in the TPCT across a broad range of r_e. The model provides accurate predictions of TPCT thermal performance, with a notably improved convergence rate in phase change simulations regardless of r values. This research is anticipated to offer valuable insights into TPCT simulation by providing a methodology for explicitly defining suitable empirical constants during the phase change process in TPCT simulations.

The Lee model was adopted as a phase change model in all studies. $S_g = r_c\alpha_g\rho_g\frac{(T-T_{sat})}{T_{sat}}$ for condensation $(T < T_{sat})$, $S_f = r_e\alpha_f\rho_f\frac{(T-T_{sat})}{T_{sat}}$ for evaporation$(T > T_{sat})$.

2. Computational methods

2.1. Governing equations

We adopted the volume-of-fluid (VOF) [35] for phase-change simulation using a commercial open-source package, OpenFOAM v2106. The governing equations and volume fraction equation are as follows:

Volume fraction equation:

$$\frac{\partial\alpha_f}{\partial t} + \nabla\cdot(\alpha_f u) + \nabla\cdot(\alpha_f\alpha_g u_r) = \alpha_f\nabla\cdot u - \alpha_f\left(\frac{\dot{\rho}}{\rho_f} - \frac{\dot{\rho}}{\rho_g}\right) + \frac{\dot{\rho}}{\rho_f} \tag{1}$$

Continuity equation:

$$\nabla\cdot u = \frac{S}{\rho_f} - \frac{S}{\rho_g} \tag{2}$$

Momentum equation:

$$\frac{\partial(\rho u)}{\partial t} + \nabla(\rho uu) = -\nabla P + \nabla\cdot\left[\mu\left(\nabla u + \nabla u^T\right)\right] + \rho\vec{g} + \sigma\kappa(\alpha)\mathbf{n}|\nabla\alpha|\frac{2\rho}{\rho_g + \rho_f} \tag{3}$$

Energy equation:

$$\frac{\partial(\rho C_p T)}{\partial t} + \nabla\cdot(\rho C_p uT) - \nabla\cdot(k_{eff}\nabla T) = Q \tag{4}$$

The volume fraction and continuity equations contain a mass source term, S, which determines the amount of mass that is affected by evaporation or condensation. The last term of the volume fraction equation, $\nabla\cdot(\alpha_f\alpha_g u_r)$, is a compression term and serves the purpose of preventing numerical divergence during calculations while simultaneously achieving a finer interface resolution [36]. u_r is the relative velocity defined as $u_f - u_g$. The inclusion of surface tension at the interface is accomplished by utilising the continuum surface force model, which is applied in the final term of the right-hand side of the momentum Eq. [37]. The curvature of the interface is established by the gradient of a volume fraction as shown below. To mitigate significant spatial oscillations, we employed the Ferrari and Lunati model [38] for defining the interface curvature, denoted as κ:

$$\kappa(\alpha) = -(\nabla\cdot\mathbf{n}) = -\left(\nabla\cdot\frac{\nabla a}{|\nabla\alpha|}\right) \tag{5}$$

In the energy equation, Q is a heat-transfer term corresponding to evaporation or condensation. The properties are determined as the volume-averaged value as follows:

$$\rho = \alpha_f\rho_f + (1-\alpha_f)\rho_g \tag{6}$$

$$\mu = \alpha_f\mu_f + (1-\alpha_f)\mu_g \tag{7}$$

$$C_P = \alpha_f C_{P,f} + (1-\alpha_f)C_{P,g} \tag{8}$$

$$k_{eff} = \alpha_f k_f + (1-\alpha_f)k_g \tag{9}$$

2.2. Phase-change model

We adopted the Lee model for the phase-change process within the TPCT for computing the mass-transfer rate and subsequently calculated the energy transfer rate as follows:

$$S_g = r_c\alpha_g\rho_g\frac{(T-T_{sat})}{T_{sat}} \text{ for condensation } (T < T_{sat}) \tag{10}$$

$$S_f = r_e\alpha_f\rho_f\frac{(T-T_{sat})}{T_{sat}} \text{ for evaporation } (T > T_{sat}) \tag{11}$$

$$Q_g = S_g h_{fg} \text{ for condensation } (T < T_{sat}) \tag{12}$$

$$Q_f = S_f h_{fg} \text{ for evaporation } (T > T_{sat}) \tag{13}$$

The subscripts g and f respectively refer to the vapour and liquid phases, corresponding to condensation and evaporation mass transfer, respectively. The variable S [kg/m^3/s] represents the mass source resulting from either condensation and evaporation mass-transfer rates. This is equivalent to the S term in Eq. (2). The variables α and ρ are dimensionless volume fraction and density, respectively, and h_{fg} [J/kg] is the latent heat. The variable Q [W/m^3] represents the corresponding heat transfer resulting from condensation and evaporation mass transfer. r_c and r_e [s^{-1}] represent the mass transfer intensity factors for condensation and evaporation, respectively.

This study proposes the redefinition of the empirical constant r_c as a variable dependent on r_e, establishing a connection between these two independent constants according to a mass balance approach within a closed TPCT system. The premise is rooted in the notion that the evaporation and condensation mass-transfer rates become equal once the closed system, including the TPCT, attains a steady-state condition. The detailed relationship is expressed as Eq. (14):

$$\sum_1^{n.e}\dot{m}_{e.cell} = \sum_1^{n.c}\dot{m}_{c.cell} \tag{14}$$

where $\dot{m}$ denotes the mass transfer rate. The summations on either side denote the cumulative sum within individual cells, where the LHS indicates total evaporative mass-transfer rate and the RHS indicates the total condensate mass-transfer rate. The definition of the mass transfer rate can be achieved using the Lee model as given by Eq. (15):

$$\sum_1^{n}\dot{m}_{cell} = \left\{\frac{r\alpha\rho(T-T_{sat})}{T_{sat}}\right\}_{cell.1} + \left\{\frac{r\alpha\rho(T-T_{sat})}{T_{sat}}\right\}_{cell.2} + \cdots + \left\{\frac{r\alpha\rho(T-T_{sat})}{T_{sat}}\right\}_{cell.n} = r\times\sum_1^{n}\left\{\frac{\alpha\rho(T-T_{sat})}{T_{sat}}\right\}_{cell} \tag{15}$$

Then, r_c can be obtained by combining Eq. (14) and Eq. (15):

$$r_c = r_e\times\sum_1^{n.e}\left\{\frac{\alpha_l\rho_l(T-T_{sat})}{T_{sat}}\right\}_{e.cell}\Bigg/\sum_1^{n.c}\left\{\frac{\alpha_v\rho_v(T_{sat}-T)}{T_{sat}}\right\}_{c.cell} \tag{16}$$

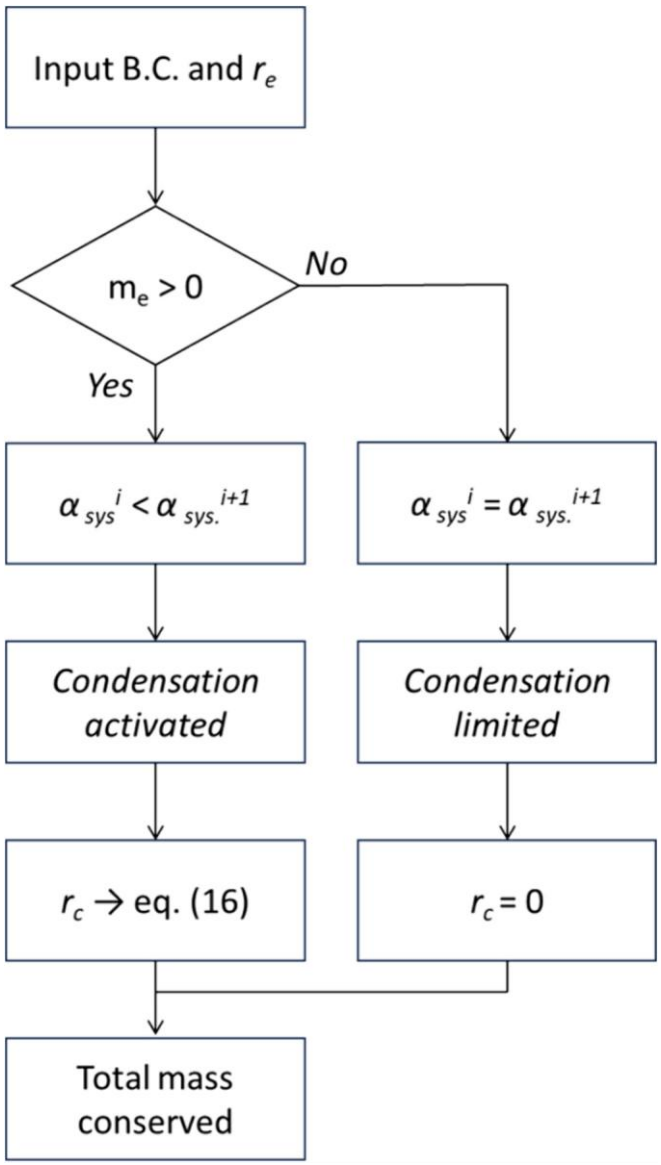

Fig. 2. Algorithm to define r_c. Once evaporation occurs at a specified r_e in the evaporator section, r_c in the condenser is explicitly defined from the evaporative mass flux.

Fig. 2 presents the algorithm for defining r_c to conserve the mass balance. When evaporation does not occur, r_c would be zero to satisfy the mass balance by limiting the condensation. By contrast, r_c would be calculated using Eq. (16) to satisfy the mass balance after evaporation occurs.

2.3. Computational domain and boundary conditions

A two-dimensional computational domain was adopted in the simulation of the TPCT as depicted in Fig. 3. The fluid domain encompasses an area of 20.2 × 400 mm^2, while the solid part is excluded because of its low thickness of 0.9 mm, leading to negligible lateral-spreading effects.

All walls are subjected to a nonslip condition. The top and bottom walls are under adiabatic conditions, whereas the evaporator section wall experiences a constant heat flux. The condenser wall is subjected to a convective heat-transfer condition with the heat-transfer coefficient. To ensure both simulation accuracy and computational efficiency, mesh independence was evaluated using three different mesh sizes: 25 k, 49 k, and 100 k. In a comparison of the average wall temperatures of the evaporator and condenser, no substantial disparities emerged between the 49 k and 100 k meshes (Fig. 4). Consequently, the 49 k mesh was chosen for implementation to strike a balance between computational efficiency and acceptable accuracy.

2.4. Solution strategy and thermophysical properties

The phase-change simulation was conducted by modifying the embedded solve, interCondensatingEvaporatingFoam in the OpenFOAM v2106. The governing equations were discretised using the VOF Method. For pressure–velocity coupling, the PIMPLE algorithm, in which the pressure implicit with splitting of operator (PISO) loop is inserted in the semi-implicit method for pressure-linked equations (SIMPLE) algorithm, was adopted. MULES was used to discretise the volume fraction equation, which could restrict the volume fraction. Equations related to time and space were solved using both first- and second-order schemes. The convergence criterion was set to 10^{-6} for velocity, 10^{-6} for pressure, 10^{-8} for volume fraction, and 10^{-10} for temperature. The time step was set to 10^{-6} s, and the maximum Courant number was 1. A relaxation factor of 1 was used for all calculations. For more detailed information, please refer to supporting information Table S1. The detailed thermophysical properties according to NIST REFPROP [39] are given in Table S2. Surface tension was set to vary corresponding to a temperature-dependent property (Please refer Table S3). Meanwhile, other properties were defined as constant values.

3. Results and discussion

3.1. Validation of the proposed method

The computational results obtained using the proposed method were compared with experimental data. To validate the proposed model, experimental data from Abdullahi's study [40] were utilised. Abdullahi's research exhibited high experimental accuracy, featuring a relatively low heat flux and a shorter TPCT length aligning with the expectation of reduced computational expenses. To evaluate whether the simulation reached a steady state, two criteria were assessed from both thermal and fluid flow perspectives. Fig. 5(a) illustrates the evaluation of the steady state from a thermal perspective, showing the time-dependent wall temperatures of the evaporator and condenser, $T_{w.e}$ and $T_{w.c}$, respectively. Both $T_{w.e}$ and $T_{w.c}$ exhibited the most significant temperature change of approximately 5 K during the first 20 s after the simulation started. However, after 20 s, $T_{w.e}$ remained around 377–378 K. In the range of 300–400 s, the temperature difference of the evaporator wall, $\Delta T_{w.e}$, was <0.5 K, confirming the steady state. Similarly, $T_{w.c}$ remained at approximately 299.4 K, and in the 300–400 s range, the temperature difference of the condenser wall, $\Delta T_{w.c}$, was <0.3 K, indicating the steady state. Furthermore, to confirm the realisation of the steady state from a fluid flow perspective, we observed the growth of the condensed liquid. Fig. 5(b) illustrates the fluid flow on the condenser wall over time. Initially, from 0 to 100 s, liquid droplets formed and grew on the wall. Around 200 s, as the droplets grew, they began to merge, resulting in larger droplets. By approximately 300 s, because of the force of gravity, the liquid started falling into the evaporator, where it regrew, repeating the cycle. This flow pattern persisted consistently from 300 s until around 400 s, confirming the attainment of the steady state.

The inner pressure of TPCT and heat balance over time is shown in the Fig. 6. The heat balance was calculated using eq. (17):

$$heat\ balance = \frac{Q_{out}}{Q_{in}} = \frac{h_c A_c \left(T_a - T_{w.c}\right)}{q'' A_e} \tag{17}$$

where Q_{in} and Q_{out} denote the total heat input and output of the TPCT system, respectively. The parameters h_c and T_a represent the heat

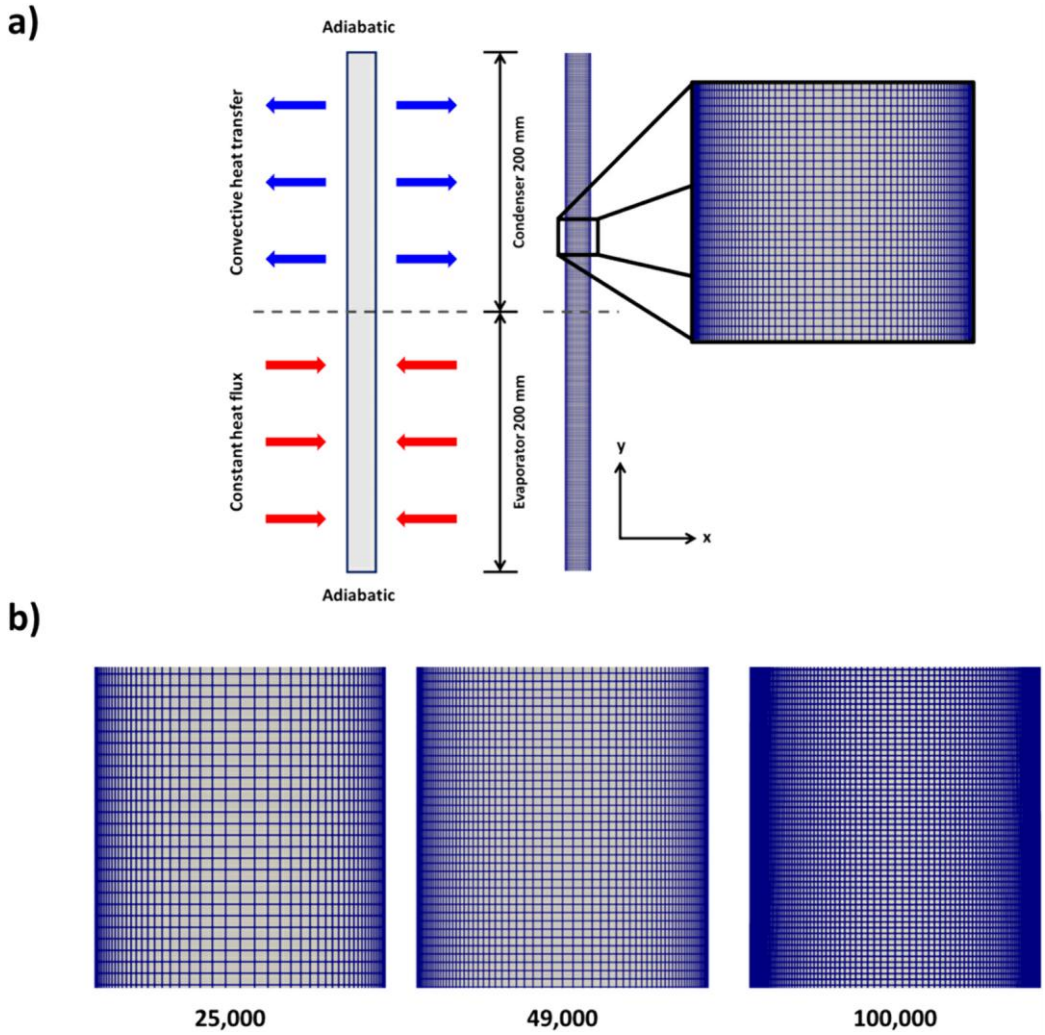

Fig. 3. Computational domain and schematic diagram of the mesh. a) Constant heat flux boundary condition on the evaporator wall and convective heat-transfer coefficient condition on the condenser section were adopted. b) Mesh images of 25 k–100 k for the mesh independent test.

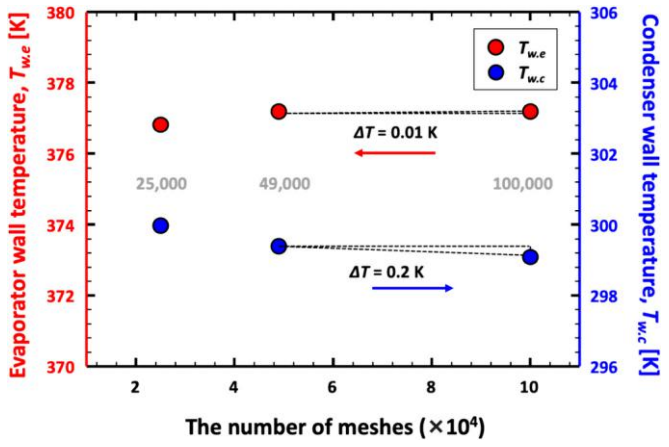

Fig. 4. Mesh independent test. Evaporator and condenser wall show temperature differences of 0.01 K and 0.2 K between 49 k and 100 k, respectively.

transfer coefficient applied to the condenser and the ambient temperature, respectively. $T_{w.c}$ denotes the average wall temperature of the condenser, while A_c and A_e denote the areas of the condenser and evaporator, respectively, which are inversely proportional to each other. Here, h_c = 405 W/m^{2}K, T_a = 293.3 K, and q'' = 2858 W/m^2 were employed. Initially, the heat balance started near zero due to initial boundary conditions at the onset of the simulation, but it sharply increased until 40 s. Despite transient fluctuations caused by the movement of bubbles and condensed liquid, the system was deemed stable, as a 1 °C change in $T_{w.c}$, led to a heat balance of approximately 0.86. Fig. S1 in the supporting information summarizes the detailed changes in heat balance for r_e ranging from 0.1 to 100 s^{-1}.

Regarding the inner pressure of the TPCT system, which reflects the average pressure across all cells, there was an initial slight increase at the beginning of the simulation, attributed to the dynamics of bubbles and condensed liquid. However, it quickly reached steady-state and subsequently fluctuated around ±0.1 kPa, stabilizing at approximately 99.0 kPa.

Fig. 7 compares the temperature distributions for the case with a heat flux of 2858 W/m^2 at the evaporator wall, while a convective heat-transfer condition with a heat-transfer coefficient of 405 W/m^{2}K was applied to the condenser wall. The ambient temperature was set to 293.3 K. The r_e used for validation was set to 0.1 s^{-1}, which is the most widely adopted value, and r_c was explicitly defined using Eq. (16) as mentioned above. During the transient simulation, the temperature reached a steady state at approximately 300 s. For an accurate comparison, the average wall temperatures for the 100 s after the simulation reached the steady state were utilised. Overall, the simulation results showed excellent agreement with the experimental data. The

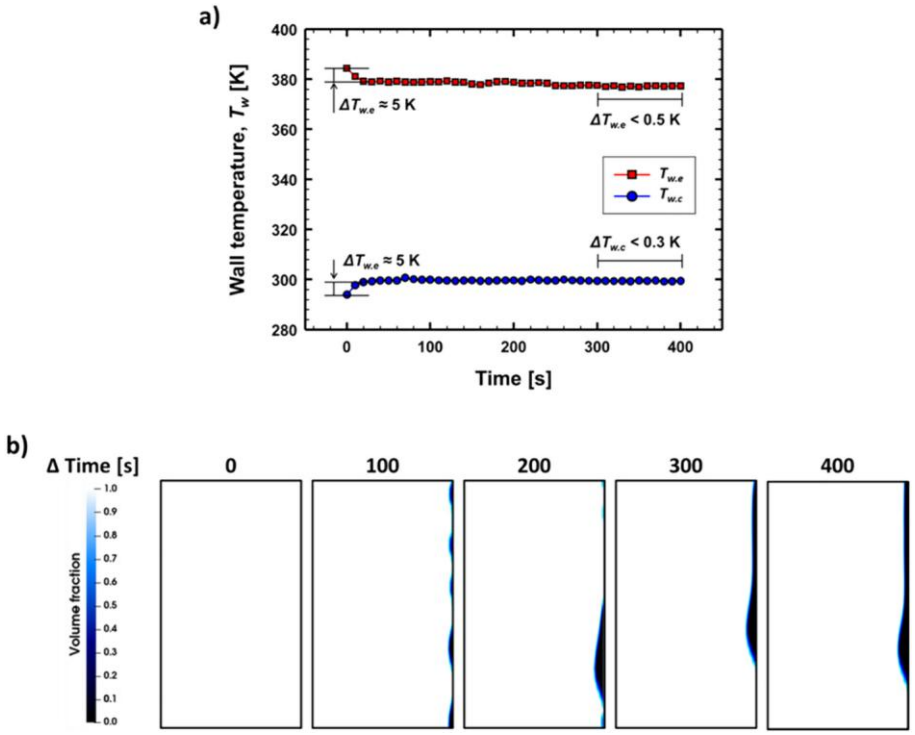

Fig. 5. Temporal variations in simulation results. a) Wall temperatures of the evaporator and condenser over a simulation time of 0–400 s. b) Sequential images of the volume fraction contour on the condenser wall at 100-s intervals, up to 400 s.

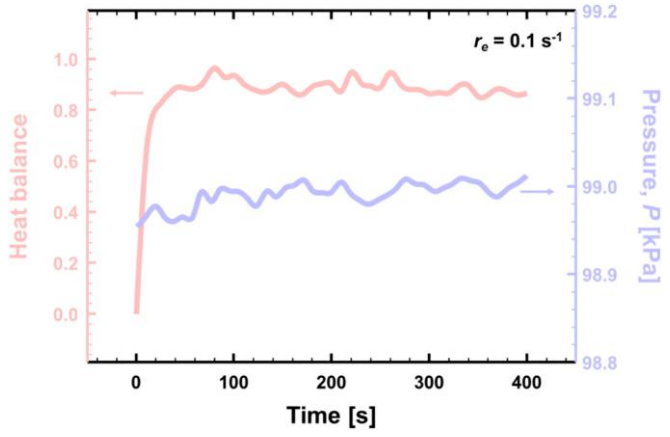

Fig. 6. Temporal changes in inner pressure and heat balance ($r_e = 0.1$ s^{-1}). The heat balance exhibited a sharp increase and stabilized around 0.86 after reaching steady-state, while the inner pressure showed a slight increase and stabilized around 99.0 kPa.

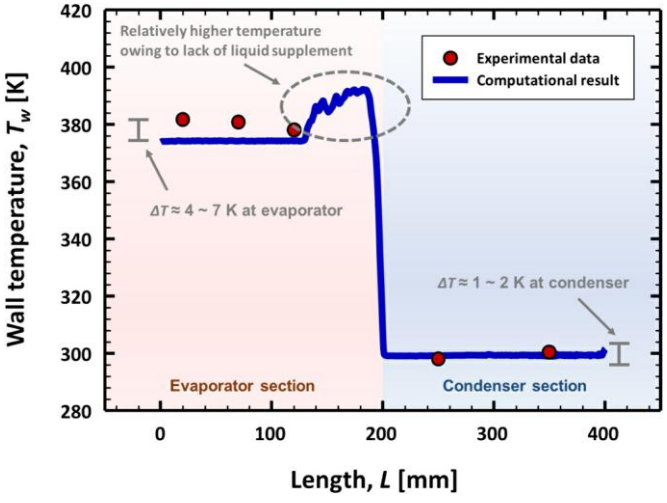

Fig. 7. Comparison between experimental and validated computational results. High accuracy of prediction is observed with a temperature difference of 1–2 K on the condenser section and 4–7 K on the evaporator section. A higher temperature was captured on the upper evaporator section.

temperature distribution in the evaporator section showed high accuracy with a temperature difference of approximately 4–7 K. However, slightly higher temperature predictions (up to ~12 K) were observed in the upper side in the evaporator section compared to the experimental data. This was attributed to droplets falling from the condenser section into the evaporator section, which caused the droplets to be slightly separated from the evaporator section owing to evaporation that occurred at the interface. Consequently, the upper side in the evaporator section had a slightly increased temperature. The condenser section showed a sharp difference in temperature and exhibited excellent accuracy ($\Delta T < 2$ K).

Fig. 8 presents a comprehensive analysis of the fluid flow within the TPCT obtained using the proposed model. Fig. 8(a) shows the volume fraction contour of the entire TPCT, droplets, and temperature of the liquid–vapour interface. In the evaporator section, the working fluid is vaporised as heat flux is applied. Subsequently, the absorbed heat is released in the condenser section in the form of droplets. As indicated by the volume fraction and temperature distribution in region A, the temperature at the liquid–vapour interface is maintained at ~335 K in the condenser region and 373 K in the evaporator region. This is because the droplet is continuously cooled by the heat dissipation of the condenser until it falls down to the condenser, while the bubble is detached from the evaporator wall and does not absorb heat from it. Fig. 8(b) presents the evolution of volume fraction at various time intervals. Initially, at 0

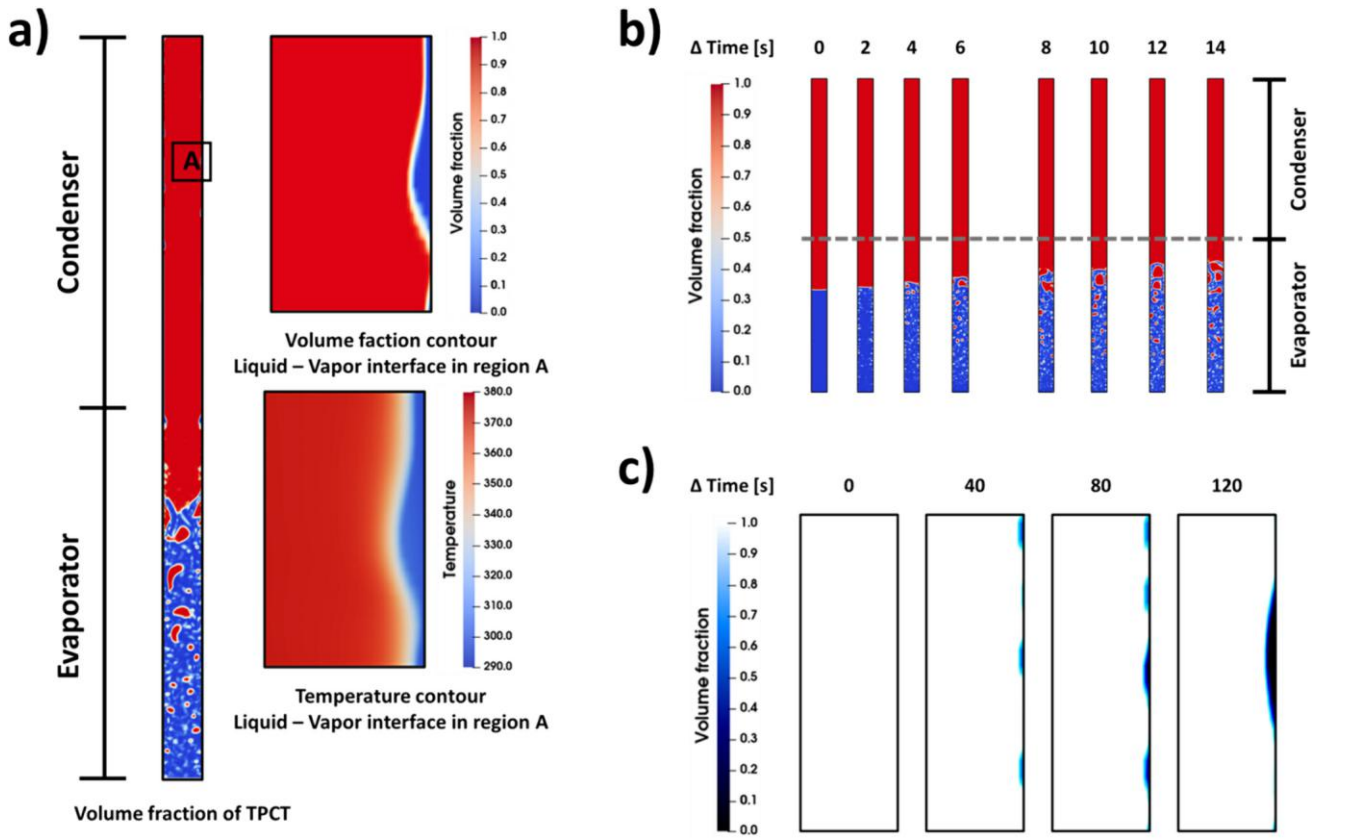

Fig. 8. Comprehensive analysis of fluid flow within the TPCT. a) Contour of volume fraction in the TPCT and detailed temperature distribution within region A, b) Evolution of volume fraction at various time intervals, and c) Magnified volume fraction in condensation flow at different instants of time.

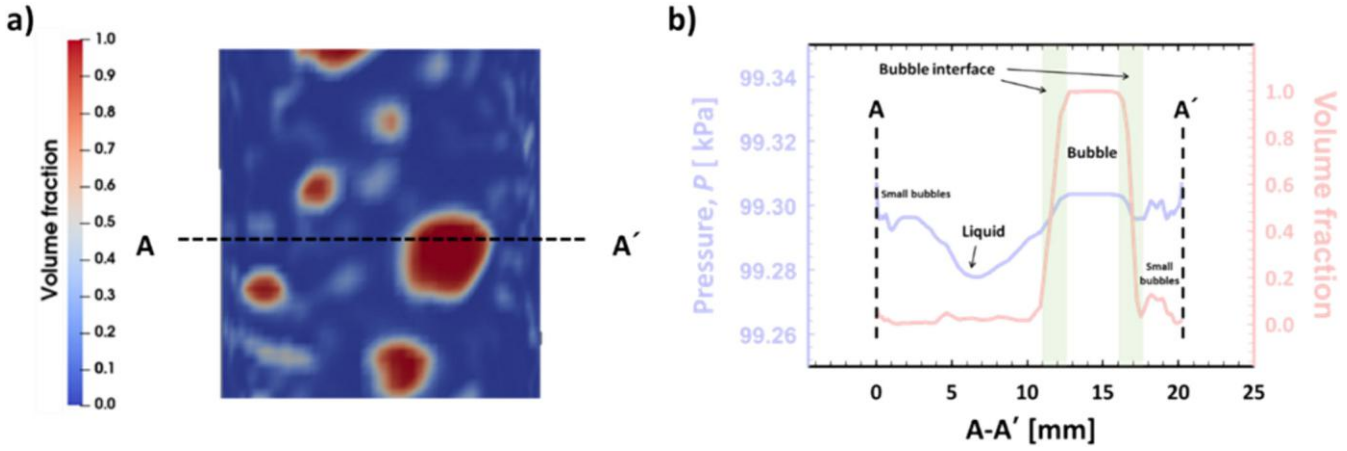

Fig. 9. Bubble evolution in the evaporator section. a) Volume faction contour of the evaporator section after the steady state with the cross section of line A-A′, b) pressure and volume fraction contour corresponding to the cross section of line A-A′.

s, there is no boiling activity in the working fluid. However, upon receiving heat, small bubbles emerge from the wall. These small bubbles coalesce and become larger bubbles, rising towards the condenser section, driven by the dominant gravitational force rather than surface tension. Fig. 8(c) shows the growth of liquid droplets in the condenser section over time. Similar to the evaporator section, no liquid droplets are observed at 0 s. However, isolated small separate droplets start to condense at widely spaced intervals, after which they become more densely distributed. These droplets then coalesce with neighbouring ones, growing in size until they eventually descend into the evaporator section under the influence of gravity.

Fig. 9(a) illustrates the volume fraction in the evaporator section of the TPCT system after reaching the steady state. A cross-sectional line A-A′ passing through the liquid and vapour within the evaporator was selected for analysis. Fig. 9(b) depicts the pressure and volume fraction along line A-A′. Overall, the pressure was approximately 99.3 kPa, showing high accuracy with a deviation of only ~1.7% from the pressure corresponding to the saturation temperature used for validation, which is 101 kPa at 373 K [40]. Additionally, owing to surface tension, the pressure distribution within the bubbles was slightly higher than that in the liquid region.

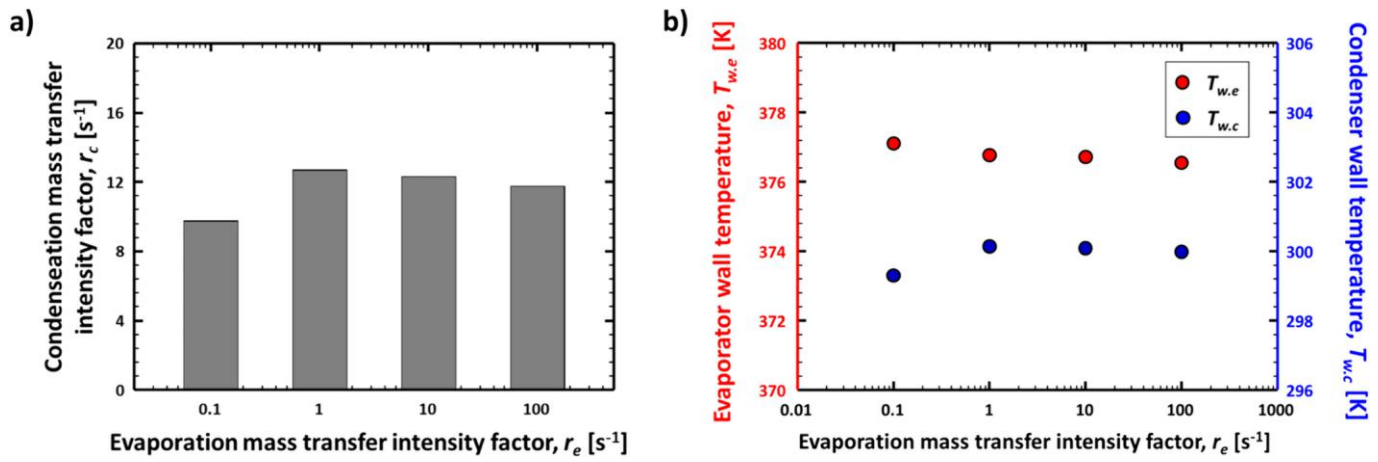

Fig. 10. Effect of different evaporator mass-transfer intensity factors on condensation mass transfer intensity factor and corresponding wall temperature changes. (a) Variations in r_c with r_e spanning from 0.1 to 100 s^{-1}. (b) Associated wall temperature changes in both evaporator and condenser sections. For $r_e \geq 1$ s^{-1}, the condensation mass-transfer intensity factor approaches near-saturation levels, resulting in consistent wall temperatures with variations of <0.8 K in both the evaporator and condenser sections.

3.2. Variations in explicitly defined r_c relative to different r_e values

After r_c is replaced as a functional value based on r_e, there remains one empirical constant, r_e. Hence, this chapter scrutinises the fluctuations in explicitly defined r_c and the associated variations in temperature distribution with respect to different r_e values. Fig. 10(a) illustrates how the explicitly defined r_c fluctuates as r_e ranges from 0.1 to 100 s^{-1}, which is 1000 times higher than the minimum value. With increasing values of r_e, r_c shows a rise but reaches a point of saturation beyond a certain value of r_e. For $r_e = 0.1$ s^{-1}, which is the most widely adopted value, r_c is specified to be 9.8 s^{-1}. When r_e is increased tenfold to 1 s^{-1}, r_c is defined to be only around 30% higher, at $r_c = 12.7$ s^{-1}. Pushing r_e further to 10 s^{-1} leads to an almost saturated value of r_c, at 12.3 s^{-1}. Further increase to $r_e = 100$ s^{-1} yields an even slightly lower value of r_c at 11.8 s^{-1}. This occurs because an increase in r_e enhances the evaporation mass-transfer rate as specified in Eq. (16). This leads to increased vapour pressure, ultimately resulting in an elevated saturated temperature within the thermosyphon. Consequently, the elevation of the saturated temperature hinders further vapour generation through evaporation, establishing equilibrium within the thermosyphon. Thus, for $r_e = 0.1$–100 s^{-1}, r_c shows a very small standard deviation of ±1.41%. Fig. 10(b) shows changes in the average wall temperature of the TPCT with different r_e values. $T_{w.e}$ represents the average wall temperature of the evaporator section, while $T_{w.c}$ pertains to the average wall temperature of the condenser section.

The average wall temperature of the evaporator section experiences a slight decrease as r_e increases. Specifically, there is only a 0.6-K difference observed for $r_e = 0.1$–100 s^{-1}, with $T_{w.e}$ shifting from 377.2 K at $r_e = 0.1$ s^{-1} to 376.6 K at $r_e = 100$ s^{-1}, attributed to the saturated r_c values at higher r_e levels. Similarly, the average wall temperature of the condenser section demonstrates consistent values, ranging from $T_{w.c} = 299.4$ K at $r_e = 0.1$ s^{-1} to $T_{w.c} = 300.0$ K at $r_e = 100$ s^{-1}, indicating a temperature difference of 0.6 K.

4. Conclusion

In this study, we propose an explicit definition model of r_c for TPCT and closed systems based on mass balance. The proposed model, which comprises the Lee model—the most widely used phase-change model—was designed to reduce two empirical constants. To validate the proposed model, TPCT simulation was conducted and validated by experimental data. It also showed high accuracy with the explicitly defined r_c. In addition, by changing r_e, the trends of the explicitly defined r_c and the temperature distribution of TPCT were analysed. The main results of this study are as follows:

1. The proposed model was able to reduce two empirical constants present in the widely used Lee model by coupling them together into a single empirical constant and dependent variable.
2. As r_e increased, r_c initially rose but saturated quickly, with $r_e = 0.1$ s^{-1} yielding $r_c = 9.8$ s^{-1}, and it further increased to $r_e = 10$ and 100 s^{-1}, leading to nearly stable values of r_c around 12 s^{-1} due to the elevated saturated temperature limiting further vapour generation and stabilizing the thermosyphon.
3. As r_e increased, $T_{w.e}$ decreased because the higher mass-transfer rate also elevated the heat-transfer rate, causing more heat to be drawn away from the wall through the evaporator section. By contrast, $T_{w.c}$ rose with an increase in r_c for the same reason.

CRediT authorship contribution statement

Sehyeon Cho: Writing – original draft, Investigation, Formal analysis, Data curation. **Dayoung Kong:** Methodology, Formal analysis, Data curation. **Gyohoon Geum:** Formal analysis, Data curation. **Seungjae Lee:** Formal analysis, Data curation. **Junrae Park:** Investigation, Formal analysis. **Seong Hyuk Lee:** Writing – review & editing, Supervision. **Jungho Lee:** Writing – review & editing, Supervision, Project administration. **Hyoungsoon Lee:** Writing – review & editing, Supervision, Project administration.

Declaration of competing interest

The authors declare that they have no known competing financial interests or personal relationships that could have appeared to influence the work reported in this paper.

Data availability

Data will be made available on request.

Acknowledgements

This work was supported by the Korea Institute of Energy Technology Evaluation and Planning (KETEP) grant funded by the Ministry of Trade, Industry & Energy, Korea. (Grant No. 20212020800270 and No. 20214000000280) and by the Chung-Ang University Graduate Research Scholarship in 2023.

Appendix A. Supplementary data

Supplementary data to this article can be found online at https://doi.org/10.1016/j.icheatmasstransfer.2024.107932.

References

[1] Y. Peng, X. Zhang, J. Liu, S. Li, Y. Mou, J. Xu, M. Chen, Waste heat recycling of high-power lighting through chips on thermoelectric generator, Energy Convers. Manag. 243 (2021) 114329, https://doi.org/10.1016/j.enconman.2021.114329.

[2] A. Takezawa, K. Makihara, N. Kogiso, M. Kitamura, Layout optimization methodology of piezoelectric transducers in energy-recycling semi-active vibration control systems, J. Sound Vib. 333 (2014) 327–344, https://doi.org/10.1016/j.jsv.2013.09.017.

[3] Y. Kim, J.S. Kim, D.H. Shin, S.M. You, J. Lee, Enhanced thermal performance of a thermosyphon for waste heat recovery: microporous coating at evaporator and hydrophobic coating at condenser, Appl. Therm. Eng. 175 (2020) 115332, https://doi.org/10.1016/j.applthermaleng.2020.115332.

[4] H. Jouhara, N. Khordehgah, S. Almahmoud, B. Delpech, A. Chauhan, S.A. Tassou, Waste heat recovery technologies and applications, Therm. Sci. Eng. Progress 6 (2018) 268–289, https://doi.org/10.1016/j.tsep.2018.04.017.

[5] S. Hossen, A.M. Morshed, A. Tikadar, A.S. Salman, T.C. Paul, Experimental investigation of heat pipe heat exchanger (HPHE) for waste heat recovery application, in: 4th Thermal and Fluids Engineering Conference, Jul. 2019, pp. 843–851.

[6] V. Safari, H. Abolghasemi, L. Darvishvand, B. Kamkari, Thermal performance investigation of concentric and eccentric shell and tube heat exchangers with different fin configurations containing phase change material, J. Energy Storage 37 (2021) 102458, https://doi.org/10.1016/j.est.2021.102458.

[7] A.A. Abbasian Arani, R. Moradi, Shell and tube heat exchanger optimization using new baffle and tube configuration, Appl. Therm. Eng. 157 (2019) 113736, https://doi.org/10.1016/j.applthermaleng.2019.113736.

[8] S.A. Nada, H.H. El-Ghetany, H.M.S. Hussein, Performance of a two-phase closed thermosyphon solar collector with a shell and tube heat exchanger, Appl. Therm. Eng. 24 (2004) 1959–1968, https://doi.org/10.1016/j.applthermaleng.2003.12.015.

[9] S.H. Noie, M.R. Sarmasti Emami, M. Khoshnoodi, Effect of inclination angle and filling ratio on thermal performance of a two-phase closed Thermosyphon under normal operating conditions, Heat Transf. Eng. 28 (4) (2007) 365–371, https://doi.org/10.1080/01457630601122997.

[10] Y. Kim, J.S. Kim, D.H. Shin, J.H. Seo, S.M. You, J. Lee, Effects of hydrophobic and superhydrophobic coatings of a condenser on the thermal performance of a two-phase closed thermosyphon, Int. J. Heat Mass Transf. 144 (2019) 118706, https://doi.org/10.1016/j.ijheatmasstransfer.2019.118706.

[11] M. Kaya, An experimental investigation on thermal efficiency of two-phase closed thermosyphon (TPCT) filled with CuO/water nanofluid, Eng. Sci. Technol. Int. J. 23 (2020) 812–820, https://doi.org/10.1016/j.jestch.2020.06.006.

[12] J.S. Kim, Y. Kim, D.H. Shin, S.M. You, J. Lee, Heat transfer and flow visualization of a two-phase closed thermosiphon using water, acetone, and HFE7100, Appl. Therm. Eng. 187 (2021) 116571, https://doi.org/10.1016/j.applthermaleng.2021.116571.

[13] A. Alizadehdakhel, M. Rahimi, A.A. Alsairafi, CFD modeling of flow and heat transfer in a thermosyphon, Int. Commun. Heat Mass Transf. 37 (2010) 312–318, https://doi.org/10.1016/j.icheatmasstransfer.2009.09.002.

[14] B. Fadhl, L.C. Wrobel, H. Jouhara, Numerical modelling of the temperature distribution in a two-phase closed thermosyphon, Appl. Therm. Eng. 60 (2013) 122–131, https://doi.org/10.1016/j.applthermaleng.2013.06.044.

[15] B. Fadhl, L.C. Wrobel, H. Jouhara, CFD modelling of a two-phase closed thermosyphon charged with R134a and R404a, Appl. Therm. Eng. 78 (2015) 482–490, https://doi.org/10.1016/j.applthermaleng.2014.12.062.

[16] J. Yuan, C. Wang, J. Zhang, J. Ling, Z. Zhou, F. Gao, Effect of non-condensable gas on thermal characteristics in two-phase closed thermosyphon, Appl. Therm. Eng. 173 (2020) 115233, https://doi.org/10.1016/j.applthermaleng.2020.115233.

[17] A.A. Alammar, R.K. Al-Dadah, S.M. Mahmoud, Numerical investigation of effect of fill ratio and inclination angle on a thermosiphon heat pipe thermal performance, Appl. Therm. Eng. 108 (2016) 1055–1065, https://doi.org/10.1016/j.applthermaleng.2016.07.163.

[18] K. Hosseinzadeh, D.D. Ganji, O. Fathollah, Effect of SiO_2 super-hydrophobic coating and self-rewetting fluid on two phase closed thermosyphon heat transfer characteristics: an experimental and numerical study, J. Mol. Liq. 315 (2020) 113748, https://doi.org/10.1016/j.molliq.2020.113748.

[19] D. Jafari, S. Filippeschi, A. Franco, P. Di Marco, Unsteady experimental and numerical analysis of a two-phase closed thermosyphon at different filling ratios, Exp. Thermal Fluid Sci. 81 (2017) 164–174, https://doi.org/10.1016/j.expthermflusci.2016.10.022.

[20] S. Ed-Dîn Fertahi, T. Bouhal, Y. Agrouaz, T. Kousksou, T. El Rhafiki, Y. Zeraouli, Performance optimization of a two-phase closed thermosyphon through CFD numerical simulations, Appl. Therm. Eng. 128 (2018) 551–563, https://doi.org/10.1016/j.applthermaleng.2017.09.049.

[21] X. Wang, Y. Wang, H. Chen, Y. Zhu, A combined CFD/visualization investigation of heat transfer behaviors during geyser boiling in two-phase closed thermosyphon, Int. J. Heat Mass Transf. 121 (2018) 703–714, https://doi.org/10.1016/j.ijheatmasstransfer.2018.01.005.

[22] X. Wang, H. Yao, J. Li, Y. Wang, Y. Zhu, Experimental and numerical investigation on heat transfer characteristics of ammonia thermosyphons at shallow geothermal temperature, Int. J. Heat Mass Transf. 136 (2019) 1147–1159, https://doi.org/10.1016/j.ijheatmasstransfer.2019.03.080.

[23] Y. Xiao, J.-W. Liu, J.-F. Zeng, X. Lu, Y. Tian, C.-M. Shu, Coupling effect of operational factors on heat extraction from a coal pile using a two-phase closed thermosyphon, Energy 239 (2022) 122371, https://doi.org/10.1016/j.energy.2021.122371.

[24] Y. Wang, X. Wang, H. Chen, R.A. Taylor, Y. Zhu, A combined CFD/visualized investigation of two-phase heat and mass transfer inside a horizontal loop thermosiphon, Int. J. Heat Mass Transf. 112 (2017) 607–619, https://doi.org/10.1016/j.ijheatmasstransfer.2017.04.132.

[25] S. Cho, D. Kong, G. Geum, S. Kang, J. Hyeuk Seo, J.S. Kim, S.H. Lee, J. Lee, H. Lee, Experimental and computational investigation of thermal performance and fluid flow in two-phase closed thermosyphon, Appl. Therm. Eng. 235 (2023) 121327, https://doi.org/10.1016/j.applthermaleng.2023.121327.

[26] Y. Kim, J. Choi, S. Kim, et al., Effects of mass transfer time relaxation parameters on condensation in a thermosyphon, J. Mech. Sci. Technol. 29 (2015) 5497–5505, https://doi.org/10.1007/s12206-015-1151-5.

[27] A. Tarokh, C. Bliss, A. Hemmati, Performance enhancement of a two-phase closed thermosyphon with a vortex generator, Appl. Therm. Eng. 182 (2021) 116092, https://doi.org/10.1016/j.applthermaleng.2020.116092.

[28] K. Kafeel, A. Turan, Simulation of the response of a thermosyphon under pulsed heat input conditions, Int. J. Therm. Sci. 80 (2014) 33–40, https://doi.org/10.1016/j.ijthermalsci.2014.01.020.

[29] Z. Xu, Y. Zhang, B. Li, J. Huang, Modeling the phase change process for a two-phase closed thermosyphon by considering transient mass transfer time relaxation parameter, Int. J. Heat Mass Transf. 101 (2016) 614–619, https://doi.org/10.1016/j.ijheatmasstransfer.2016.05.075.

[30] A.M. Al Jubori, Q.A. Jawad, Computational evaluation of thermal behavior of a wickless heat pipe under various conditions, case studies, Therm. Eng. 22 (2020) 100767, https://doi.org/10.1016/j.csite.2020.100767.

[31] W.H. Lee, A pressure iteration scheme for two-phase flow modeling, in: T. N. Veziroglu (Ed.), Multiphase Transport Fundamentals, Reactor Safety, Applications vol. 1, Hemisphere Publishing, Washington, DC, 1980.

[32] R.W. Schrage, A Theoretical Study of Interphase Mass Transfer, Columbia University Press, 1953, https://doi.org/10.7312/schr90162.

[33] G. Son, V.K. Dhir, Numerical simulation of film boiling near critical pressures with a level set method, J. Heat Transf. 120 (1998) 183–192, https://doi.org/10.1115/1.2830042.

[34] Z. Pan, J.A. Weibel, S.V. Garimella, A saturated-interface-volume phase change model for simulating flow boiling, Int. J. Heat Mass Transf. 93 (2016) 945–956, https://doi.org/10.1016/j.ijheatmasstransfer.2015.10.044.

[35] C.W. Hirt, B.D. Nichols, Volume of fluid (VOF) method for the dynamics of free boundaries, J. Comput. Phys. 39 (1981) 201–225, https://doi.org/10.1016/0021-9991(81)90145-5.

[36] E. Berberović, N.P. van Hinsberg, S. Jakirlić, I.V. Roisman, C. Tropea, Drop impact onto a liquid layer of finite thickness: dynamics of the cavity evolution, Phys. Rev. E 79 (2009) 036306.

[37] J.U. Brackbill, D.B. Kothe, C. Zemach, A continuum method for modeling surface tension, J. Comput. Phys. 100 (1992) 335–354, https://doi.org/10.1016/0021-9991(92)90240-Y.

[38] A. Ferrari, I. Lunati, Direct numerical simulations of interface dynamics to link capillary pressure and total surface energy, Adv. Water Resour. 57 (2013) 19–31, https://doi.org/10.1016/j.advwatres.2013.03.005.

[39] E.W. Lemmon, I.H. Bell, M.L. Huber, M.O. McLinden, NIST Standard Reference Database 23: Reference Fluid Thermodynamic and Transport Properties-REFPROP, Version 10.0, National Institute of Standards and Technology, 2018. http://www.nist.gov/srd/nist23.cfm.

[40] B. Abdullahi, Development and Optimization of Heat Pipe Based Compound Parabolic Collector, Thesis submitted to, University of Birmingham, 2015.